ANISOTROPIC RADIO SCATTERING OF NGC 6334B

A. S. TROTTER AND J. M. MORAN

Harvard-Smithsonian Center for Astrophysics, 60 Garden Street, Cambridge, MA 02138

AND

L. F. RODRÍGUEZ

Instituto de Astronomía, UNAM, Apdo. Postal 70-264, México, D.F. 04510, México

ABSTRACT

The extragalactic radio source NGC 6334B is the most strongly scattered object known, with an angular size of 3″ at 20 cm wavelength. Its angular size scales as the square of the observing wavelength, and its phase structure function has a power-law dependence on projected baseline length. These properties suggest that NGC 6334B is a point source, probably a quasar, scatter broadened by an intervening region of turbulent plasma. The line of sight to the source intercepts the northern lobe of the bipolar H II region NGC 6334A, which is probably the source of the scattering. We discuss observations of NGC 6334B with the VLA at 1.4, 2, 6, 20, and 90 cm, and with the VLBA at 1.4, 3.6, and 6 cm. The VLA observations indicate that the scattering disk of NGC 6334B is anisotropic, with an axial ratio of ~ 1.2 at 20 and 6 cm, and ~ 1.5 at 2 cm. This anisotropy is probably due to the effects of a magnetic field in the scattering medium. The position angle of the scattering disk implies that the mean projected magnetic field direction is parallel to the outflow from NGC 6334A. The position angle of the scattering disk rotates slightly between 6 and 2 cm; we use this rotation to place an upper limit on the outer scale of turbulence, $r_{out} \lesssim 10^{16}$ cm. We present a new algorithm to detect the presence of weak ($< 3\,\sigma$) fringes in interferometric data. Detections of low-level excess visibility on long VLBA baselines at 3.6 cm place an upper limit on the inner dissipative scale of turbulence r_{in} of 10^{11-12} cm, while the baseline scaling of fringe visibility amplitude and the wavelength scaling of scattering-disk size place a lower limit on r_{in} of 5×10^6 cm. Nearby high-velocity (-80 km s^{-1}) H$_2$O maser features show little sign of broadening, implying that they are in front of, or less than 100 pc behind, the scattering region.

Subject headings: galaxies: individual (NGC 6334B) — H II regions — ISM: individual (NGC 6334A) — ISM: magnetic fields — radio continuum: ISM — scattering

1. INTRODUCTION

There has been considerable interest in recent years in using observations of radio source scattering as a probe of the dynamics, kinematics, and distribution of turbulence in the interstellar medium (ISM; e.g., Rickett 1990). The most highly scattered radio source known is NGC 6334B, with an angular size of 3″ at a wavelength of 20 cm. The source's angular size is observed to scale as the square of the wavelength, which is the dependence expected for diffractive scattering of a point source by turbulent plasma. H I absorption spectra indicate that this source is a quasar seen through the plane of the Galaxy (Rodríguez, Cantó, & Moran 1988, hereafter RCM; Moran et al. 1990a). The line of sight to this quasar intersects NGC 6334, a large complex of molecular clouds and H II regions, at a distance of 1.7 kpc. Radio images of the region show that NGC 6334B is roughly coincident with the northern lobe of the bipolar H II region NGC 6334A (Moran et al. 1990a; RCM; De Pree et al. 1995).

In this paper, we analyze observations of NGC 6334B using the NRAO Very Large Array (VLA)[1] and Very Long Baseline Array (VLBA) to determine the shape and orientation of its scattering disk over a range of wavelengths. We looked for evidence of anisotropic scattering, information on the power-law index of turbulent plasma density fluctua-

tions, and evidence for inner and outer scales to the turbulence. We employed model fitting of complex visibility, visibility-amplitude, and closure-amplitude data, as well as Gaussian fits to the brightness profile in synthesized images. We also analyzed results of a spectral line VLBA observation of a cluster of H$_2$O masers that lies 2′ from NGC 6334B, and that may be physically associated with the material responsible for the scattering.

In § 2 we summarize the observations and initial data reduction. In § 3 we describe further calibration and model-fitting procedures used to determine the scattering-disk parameters. In § 4 we present the results of the analysis, including fitted parameters to the scattering-disk profiles and synthesized images of the scattering region. In § 5 we address the physics of the scattering medium in more detail, theoretical models of the scattering-disk phase structure function, and the statistical properties of the interferometric visibility function. Finally, in § 6 we discuss the implications of our results for models of anisotropic turbulence in the ISM, and present a model for the scattering region of NGC 6334B.

2. OBSERVATIONS AND DATA REDUCTION

In this section we present two sets of observations: multi-frequency VLA observations of NGC 6334B spanning a period of 13 yr, some of which are discussed in previous papers (Moran et al. 1990a, 1990b) and combined VLA-VLBA observations made in 1993 April that are discussed here for the first time. Information about these experiments is summarized in Table 1.

---

[1] The National Radio Astronomy Observatory (NRAO) is operated by Associated Universities, Inc., under cooperative agreement with the National Science Foundation.

TABLE 1

OBSERVATIONS OF NGC 6334B

Instrument	Date	ν (GHz)	Band	λ/D_{min} (arcsec)	λ/D_{max} (arcsec)
VLA (A array)	1981 Feb 20	4.9	C	63	0.38
VLA (A array)	1994 Apr 4	4.9	C	63	0.38
VLA (A array)	1981 Feb 20	15.0	U	21	0.12
VLA (A array)	1981 Feb 20	1.5	L	210	1.2
VLA (A array)	1981 Feb 20	22.5	K	14	0.083
VLA (B array)	1989 Mar 5	0.330	P	1250	10.6
VLBA + phased VLA......	1993 Apr 13	8.4	X	0.20	0.0046
VLBA + phased VLA......	1993 Apr 17	4.9	C	0.34	0.0079
VLBA + phased VLA......	1993 Apr 17	22.2	K	0.075	0.0017

2.1. VLA Observations

The VLA was in the A-array configuration (maximum baseline ≈ 35 km) for all of the observations except for those at P band, when it was in B array (maximum baseline ≈ 11 km). The data were recorded in both left and right circular polarization with a bandwidth of 50 MHz, except for P band, which had a bandwidth of 3.1 MHz. The data were edited and calibrated by using standard procedures in the Astronomical Image Processing System (AIPS) data reduction package, and coherently averaged in time to improve the signal-to-noise ratio (S/N). All the data were written to ASCII files with the task UVPRT. The C-, U-, and K-band data were further processed by means of FORTRAN routines we wrote. Details of these processing steps and of the model-fitting routines are discussed in § 3. The L- and P-band data were deconvolved and imaged using the maximum entropy method (MEM), as implemented in the AIPS task VTESS. NGC 6334B was not detected at P band, because the large scattering-disk size at this wavelength ($\theta_s \sim 1\farcs3$) caused it to be highly resolved on even the shortest VLA baselines (§ 4.4). In § 4 we present the results of our analysis of these VLA data.

2.2. VLBA Observations

K-, X-, and C-band observations with the VLBA were taken on 1993 April 12 and 17, when the array was in a shake-down phase. The phased VLA was also included as an array element to improve the sensitivity of the measurements. An observation was also conducted at U band (15 GHz), but because of errors in calibration it provided no useful data. We used only five of the VLBA antennas: Fort Davis, TX (FD); Los Alamos, NM (LA); North Liberty, IA (NL); Pie Town, NM (PT); and Kitt Peak, AZ (KP). This array sampled a range of baselines from 50 km (VLA-PT) to nearly 1500 km (NL) baselines. The data were recorded in standard Mk III format in both upper and lower sidebands, resulting in 14 bandpasses of 2 MHz. The data were processed with the Mk III correlator at Haystack Observatory and reduced with the AIPS data reduction package. Fringe fitting and amplitude calibration were performed on the primary calibrator, NRAO 530 (1730−130), and the solutions were interpolated in time across the NGC 6334B scans. Finally, the data were averaged in frequency to increase the signal-to-noise ratio (S/N) of the fringe visibility measurements. In § 4 we present the results of our analysis of these VLBA data.

We also made VLBA observations of an H_2O maser that is separated from NGC 6334B by only 2′ and that appears to be associated with the bipolar H II region NGC 6334A

(Moran & Rodríguez 1980). The data were processed in a 112 channel spectral line mode with a channel width of 18 kHz ($\Delta v = 0.25$ km s^{-1}). After initial fringe fitting and bandpass calibration with the continuum calibrator, we corrected residual phase errors by phase referencing to the channel of peak emission (22 Jy at $v_{LSR} = -80.4$ km s^{-1}; radio definition, $v/c = -\Delta v/v_0$). After imaging each spectral channel, we fitted elliptical Gaussian models to all peaks in the image greater than 5 σ, using the AIPS task SAD.

3. MODEL FITTING

In this section we describe the models and fitting routines used to measure the parameters of the scattering disk of NGC 6334B.

3.1. The Model

We describe the scattering disk of NGC 6334B with five parameters: the zero-spacing flux density S_0 (millijanskys); the FWHM of the major and minor axes, θ_{maj} and θ_{min} (milliarcseconds); the position angle ϕ of the major axis in the plane of the sky (degrees east of north); and the power-law index α of the visibility phase structure function (§ 5.3). The ensemble average visibility amplitude $\langle \mathcal{V} \rangle$ of the scattering disk as a function of baseline can be expressed as

$$\langle \mathcal{V} \rangle = S_0 \exp\left[\frac{-(a^2\theta_{min}^2 + b^2\theta_{maj}^2)}{C(\alpha)} \right]^{\alpha/2}, \quad (1)$$

where a and b, the components of the baseline vector along the minor and major axes of the scattering disk, respectively, are given by

$$a = u \cos \phi + v \sin \phi$$

and

$$b = v \cos \phi - u \sin \phi. \quad (2)$$

The constant $C(\alpha)$ contains unit-conversion factors and depends on the power-law index α; it is defined such that θ_{maj} and θ_{min} are equal to the FWHM of the scattering disk in the image plane. Values of $C(\alpha)$ were computed numerically and tabulated for $1 \le \alpha \le 3$. Representative values are $C(2) = 11,952$ and $C(5/3) = 9193$, for (θ_{min}, θ_{maj}) in milliarcseconds and (a, b) in megawavelengths. Note that equation (1) is valid only if the background source is unresolved in the absence of scatter broadening; otherwise, S_0 should be replaced by the source's intrinsic visibility function. Figure 1 illustrates the coordinate systems and spatial scales defined in this paper.

We note that the measured visibilities must be corrected for noise bias before comparison with models based on

FIG. 1.—Diagram illustrating the coordinate systems and scale lengths discussed in §§ 3.1 and 5.2.

equation (1). The measured visibility amplitude Z is related to the true visibility amplitude $\mathcal{V}$ by the relation $Z^2 \approx \mathcal{V}^2 + 2\sigma^2$, where σ is the rms deviation of a single component of the complex noise vector (the components of the noise vector are independent zero-mean Gaussian random variables; see Thompson, Moran, & Swenson 1986, hereafter TMS). In addition, we have developed a novel method to estimate both σ and $\mathcal{V}$ from a sample of measurements of Z. This technique is described in the Appendix, and is used in our analysis.

In performing the analysis described below, we assumed that the measured interferometric visibilities represented a true ensemble average (§ 5.3). Goodman & Narayan (1989) have demonstrated that the typical integration times of VLA and VLBI observations do not strictly meet the criteria for ensemble average visibilities on baselines r greater than the diffractive scale $r_d \approx \lambda/\theta_s$, where θ_s is the angular size of the scattering disk and λ is the observing wavelength (see § 5.2). However, for $r \lesssim r_d$, their alternative "average" visibility function closely approximates the ensemble average visibility function.

In fitting only the amplitude of the complex visibility vector, we lose information on the absolute position of the scattering disk, while in fitting closure amplitudes (§ 3.3), we lose information about the flux density (note that for a radially symmetric scattering-disk model, closure phases are zero and so provide no useful information). In fitting the parameters listed above, data from baselines on which there was significant confusing emission from the surrounding H II regions (primarily the shortest baselines of the VLA), and on which the source was heavily resolved (primarily the longest baselines of the VLBA), were discarded. To ensure that our results were not affected by the selective flagging of baselines, we performed model fits on the data with a range of inner cutoff values. We found the fitted model parameters were insensitive to the choice of inner cutoff radius, while the χ^2 of the fits improved as the confusing emission was

removed. However, because of the southerly declination of the source ($\delta = -36°$), too large an inner cutoff radius eliminated critical north-south baselines, which made the determination of the axial ratio and the position angle of the scattering disk more difficult. The inner cutoff was important primarily for the C-band VLA observations, for which we chose a value of 100 kλ. Figure 2 shows the (u, v) coverage provided by the VLA at C band. We examined the long-baseline VLBA data separately in order to determine whether there was evidence of excess root mean squared (rms) visibility amplitude, which is predicted in typical interferometric observations of scattering disks due to the incomplete realization of a true ensemble average. The amount of excess power on long baselines is a function of the details of the power spectrum of turbulent density fluctuations sampled by the observation (Goodman & Narayan 1989; Narayan & Goodman 1989; Wilkinson, Narayan, & Spencer 1994, hereafter WNS) and thus can provide constraints on such parameters as the inner dissipative scale of turbulence r_{in} and the steepness of the power spectrum. We discuss the results of our analysis of the long-baseline excess visibility in § 6.1.2.

3.2. The Fitting Routine

Model fitting that used the model of equation (1) was performed with standard χ^2 minimization techniques. There are several algorithms available that can be used to minimize χ^2 with respect to a set of model parameters. We chose to use the "downhill simplex" minimization technique, as implemented by the subroutine amoeba (Press et al. 1992). This method had the advantage that, for our nonlinear model, it was better able to avoid converging on shallow local minima in χ^2 space than was the more formal Levenberg-Marquardt algorithm. A disadvantage is that amoeba does not produce any theoretical error estimates for the fitted parameters. We overcame this deficiency by using a Monte Carlo "bootstrap," or resampling, technique.

FIG. 2.—The (u, v) coverage of the 1994 VLA C-band observation. Data from the inner 100 kλ was suppressed to reduce confusion from extended H II emission in NGC 6334.

In this technique the errors in the model parameters describing a data set can be well estimated from the actual distribution of measured data points. It is implemented by model fitting to a number of duplicate data sets, each created by selecting a number of points at random from the original data set. The selection is performed with replacement, so that a given point in the original data can appear more than once in the resampled data. We ran our fitting routines to convergence on such ensembles (typically 200–10,000 sets), and used the resulting fitted parameter distribution to estimate the uncertainties in the scattering-disk parameters. The ensemble of fitted parameters was found generally to have a normal distribution, so the quoted error is the 1 σ full width of a Gaussian fit to a histogram of the Monte Carlo results for a given parameter. Tests with simulated data sets indicate that this bootstrap method determines the errors in the scattering-disk parameters accurately.

3.3. Closure Amplitudes

Besides the measurement errors discussed above, each visibility amplitude also has a time-dependent systematic error. It is typical to assume that the complex multiplicative gain factor G_{nm} on a baseline between antennas n and m is the product of two independent antenna gains, $G_{nm} = g_n g_m^*$. The effect of time-variable antenna gains can be removed by using closure amplitudes. The visibility amplitudes on four baselines connecting four antennas can be combined to form a closure amplitude $\mathscr{A}$ given by

$$\mathscr{A} \equiv \frac{\mathscr{V}_{12}\,\mathscr{V}_{34}}{\mathscr{V}_{23}\,\mathscr{V}_{41}}, \tag{3}$$

where $\mathscr{V}_{nm}$ is the (bias-corrected) amplitude on the baseline connecting antennas n and m. The closure amplitude is independent of the flux density of the source being modeled. On the other hand, the fitted value of the power-law index α of the phase structure function is generally very sensitive to the zero-spacing flux density estimate (Desai, Gwinn, & Diamond 1994; Desai 1995; WNS). We therefore used closure-amplitude fits to confirm the value of α given by fits to the visibility amplitude.

The use of closure amplitudes in model fitting is complicated by the fact that a value of $\mathscr{A}$ computed from measured visibilities with equation (3) will be biased to a value $\mathscr{A}'$, since the computation involves taking the reciprocal of quantities that have intrinsic measurement errors. It is also difficult to define the error $\sigma_{\mathscr{A}}$ associated with a closure-amplitude point so that the χ^2 statistic will be meaningful. From first-order expansion it can be shown that a given closure-amplitude point will have a bias given by

$$\mathscr{A}' \approx \mathscr{A}\left(1 + \frac{\sigma_{23}^2}{\mathscr{V}_{23}^2} + \frac{\sigma_{41}^2}{\mathscr{V}_{41}^2}\right), \tag{4}$$

and an error given by

$$\sigma_{\mathscr{A}}^2 \approx \mathscr{A}^2\left(\frac{\sigma_{12}^2}{\mathscr{V}_{12}^2} + \frac{\sigma_{23}^2}{\mathscr{V}_{23}^2} + \frac{\sigma_{34}^2}{\mathscr{V}_{34}^2} + \frac{\sigma_{41}^2}{\mathscr{V}_{41}^2}\right), \tag{5}$$

where σ_{nm} is the measurement error of $\mathscr{V}_{nm}$ (approximately $2^{1/2}\,\sigma$ for high-S/N points). These expressions were derived on the assumption that $s \gg 1$ for each of the four visibilities. If the S/N ratio of one of the visibilities in equation (3) is low, these expressions do not apply, and it becomes very

difficult to estimate the closure-amplitude bias and error. Hence, closure-amplitude fitting was restricted to the highest S/N data from the VLA.

4. RESULTS OF MODEL FITTING

In this section we present the results of various estimates and model fits of the parameters of the scattering disk of NGC 6334B, made from the VLA and VLBA observations described in § 2. The subsections are organized by wavelength.

4.1. C Band

We performed visibility-amplitude and closure-amplitude fits to the 1981 and 1994 VLA C-band observations. Figure 3 shows the 1994 visibility amplitudes versus baseline length. The data from 1981 are similar, except that the total flux density of NGC 6334B was 815 as opposed to 470 mJy, a change of more than 40% over 13 yr. This variation may be an effect of refractive scintillation (see § 5.2).

The results of the VLA C-band fits are summarized in Table 2. The scattering disk is found to have an elongated profile, with an axial ratio $\rho \equiv \theta_{\mathrm{maj}}/\theta_{\mathrm{min}} = 1.2$, oriented nearly east-west in the plane of the sky. For reference, the line of Galactic latitude $b = +0°40'39''$ intercepts NGC 6334B at a position angle $\phi_b = 48°.9$. Figure 4 shows the 1994 C-band visibility amplitude along two different position angles in the (u, v)-plane. This plot was produced by selecting the visibility amplitudes in two perpendicular 20° wide "wedges," and averaging them in radial bins within each wedge. The elongation of the scattering disk is clearly demonstrated; the east-west baselines show consistently lower visibilities than do the north-south baselines of the same projected length. The closure-amplitude model fits yielded a power-law index for the phase structure function of $\alpha = 1.94 \pm 0.03$ for the 1981 observation, and 1.95 ± 0.02 for the 1994 observation, consistent with the values obtained from the visibility-amplitude fits. Hence, we are
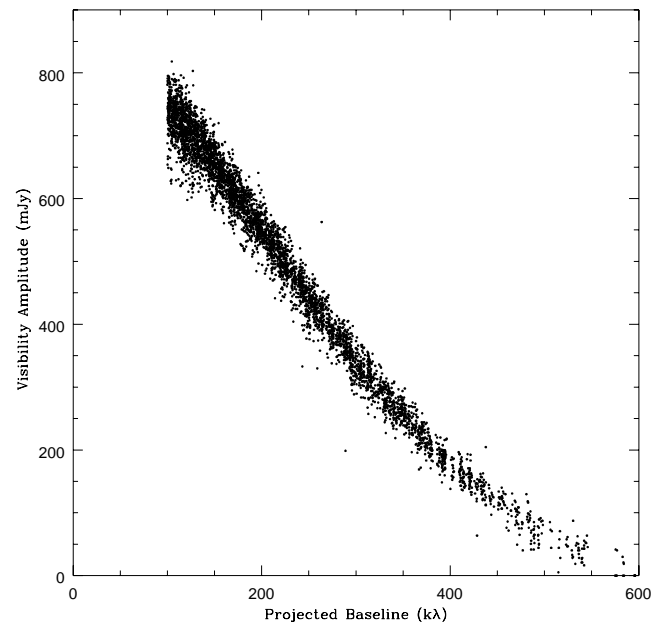

FIG. 3.—VLA C-band visibility amplitudes vs. projected baseline length (in kλ) for data taken in 1981 February. Data from the inner 100 kλ of the (u, v)-plane was suppressed to reduce confusion from extended emission.

TABLE 2

FITTED PARAMETERS TO VLA C-BAND OBSERVATIONS

Parameters	Visibility Amplitude	Closure Amplitude
VLA-C81		
θ_{maj} (mas).....................	342 ± 1	336 ± 3
θ_{min} (mas).....................	270 ± 2	277 ± 12
ρ	1.27 ± 0.01	1.21 ± 0.05
ϕ (degrees east of north)......	87.1 ± 0.4	87 ± 2
S_0 (mJy)	814 ± 3	...
α................................	1.94 ± 0.01	1.94 ± 0.03
VLA-C94		
θ_{maj} (mas).....................	338 ± 2	338 ± 1
θ_{min} (mas).....................	273 ± 7	281 ± 11
ρ	1.24 ± 0.03	1.20 ± 0.05
ϕ (degrees east of north)......	91 ± 1	88 ± 2
S_0 (mJy)	469 ± 5	...
α................................	1.95 ± 0.03	1.95 ± 0.02

confident that the anisotropy is not an artifact of an array calibration problem.

Figure 5 is a plot of $\log_{10} (-\ln \mathcal{V})$ versus $\log_{10} (r/r_d)$ binned along the 20° wide east-west wedge. The visibilities have been normalized by the zero-spacing flux density determined from the visibility-amplitude fit listed in Table 2. This choice of axes allows us to see the dependence of the phase structure function (§ 5.2) on baseline length. The straight line represents the best linear fit to the binned data points; its slope corresponds to $\alpha = 1.93 \pm 0.01$. The uncertainty in the slope is primarily due to uncertainty in S_0 (see Desai 1995). WNS found that the slope of the best-fit line to such a log-log plot of the structure function tends to be biased to lower values if the points are produced by averaging the visibilities of an elliptical source over a range of position angles in the (u, v)-plane. We therefore believe this power-law index measurement is consistent with the value

$\alpha = 1.95$ determined from elliptical model fits to the visibility and closure amplitudes.

We did not detect fringes on NGC 6334B at C band with the VLBA + VLA array. We did not expect to see the 300 mas scattering disk because it is highly resolved on even the shortest VLBA baselines. Estimation of the S/N on the most sensitive ($\sigma \approx 10$ mJy) VLBA-VLA baselines, using the algorithm described in the Appendix, yielded no evidence of any flux density at greater than the 2 σ level. Assuming a zero-spacing flux density comparable to that observed with the VLA in 1994 April ($S_0 = 470$ mJy), we place an upper limit on the level of long-baseline residual fringe visibility at C band of about 4% of the total flux density.

4.2. U Band

At U band the scattering disk is only slightly resolved on the longest VLA A-array projected baselines (Fig. 6), so
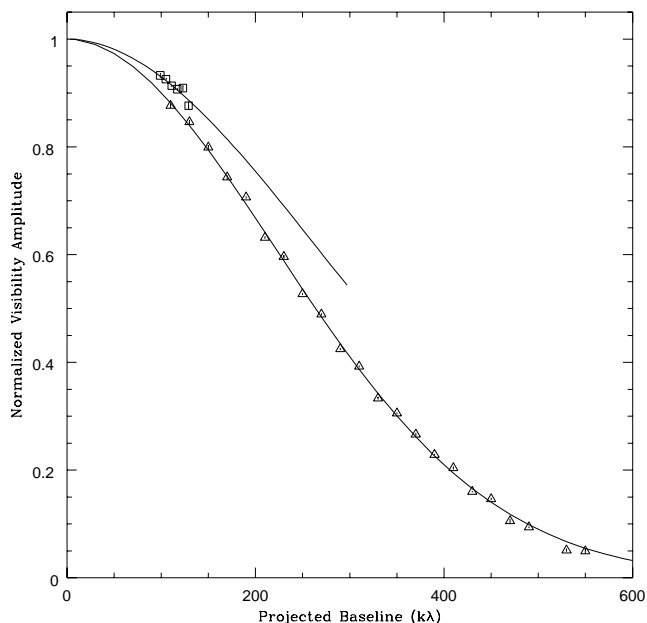
FIG. 4.—Bin-averaged VLA C-band visibility amplitudes vs. baseline, from the observation of 1981. Triangles mark points lying in a 20° wide wedge centered on $\phi = +90°$ (east-west wedge). Squares are for an identical wedge oriented north-south. The solid curves correspond to the best-fit elliptical power-law model (Table 2).
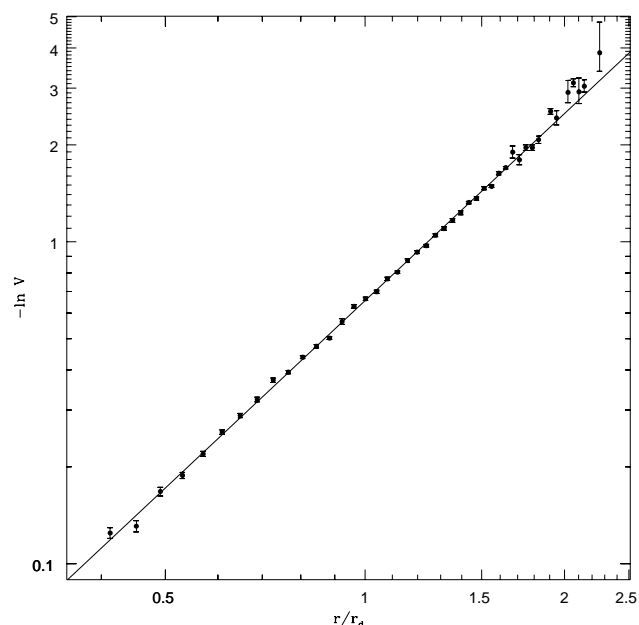
FIG. 5.—Plot of $-\ln \mathcal{V}$ vs. r/r_d along the east-west wedge of Fig. 5. In this case, $r_d \approx 16$ km. The solid line is the best least-squares fit to the binned points. The slope of the line corresponds to the power-law index α of the phase structure function. In this case, $\alpha = 1.93 \pm 0.01$.
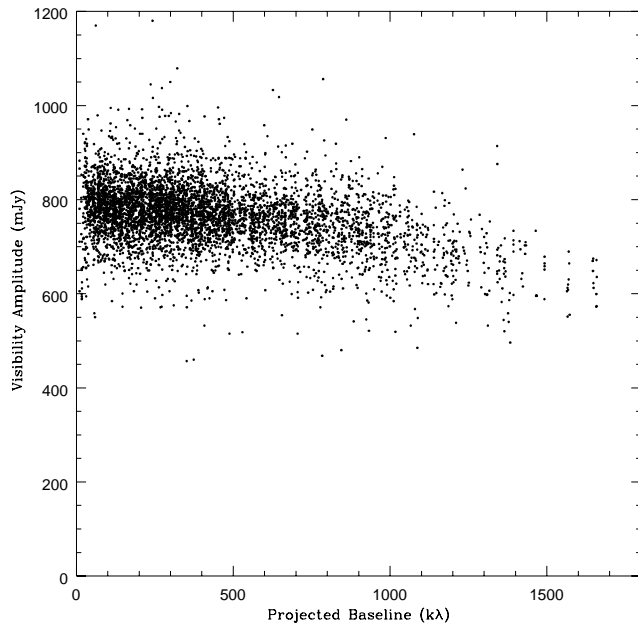
FIG. 6.—U-band visibility amplitudes vs. projected baseline length, measured in 1981 February with the VLA.

removal of antenna-based amplitude gain errors is particularly important in determining the scattering-disk parameters accurately. The fit to the closure amplitudes gave a scattering disk with major axis $\theta_{maj} = 35.6 \pm 1.6$ mas, minor axis $\theta_{min} = 25 \pm 6$ mas, and position angle $\phi = 55° \pm 13°$. The power-law index was held fixed at $\alpha = 1.95$ so that the fitted FWHM scattering-disk size could be compared directly with that determined at C band. Note that the scattering-disk shape and orientation appear to change between $\lambda = 6$ cm and $\lambda = 2$ cm; the ellipticity is slightly greater ($\rho \sim 1.5$), and the position angle has rotated by approximately 30°. Table 3 summarizes this closure-amplitude result as well as the result of visibility-amplitude fits. Figure 7 shows the same type of (u, v) wedge plot for U band as used in Figure 4. As at C band, visibilities tend to be higher on north-south than on east-west projected baselines of comparable length, although the anisotropy is less obvious in the U-band wedge plot due to lack of resolution of the scattering disk.

4.3. K Band

At the K band NGC 6334B is only barely resolved by the VLA. Attempts to fit elliptical models to the closure amplitudes generally converged to a point-source solution. At

TABLE 3
FITTED PARAMETERS TO VLA U-BAND OBSERVATIONS

Parameters	Visibility Amplitude	Closure Amplitude
θ_{maj} (mas)....................	34 ± 1	36 ± 2
θ_{min} (mas)....................	23 ± 5	25 ± 6
ρ	1.5 ± 0.3	1.4 ± 0.4
ϕ (degrees east of north)......	63 ± 12	55 ± 13
S_0 (mJy)	785 ± 3	...
α[a]	1.95	1.95

[a] α held fixed at 1.95.

C band, $\theta_s \sim 300$ mas, so assuming a λ^2 scaling relation, the expected size at K band would be about 15 mas. We were able to fit a circularly symmetrical model to the amplitudes and closure amplitudes; the results are presented in Table 4.

We used the algorithm described in the Appendix to estimate S/N and the value of σ in the VLBA K-band visibility data set for each scan on each baseline. The only detection above the 2 σ (100 mJy) level was on the PT-VLA baseline
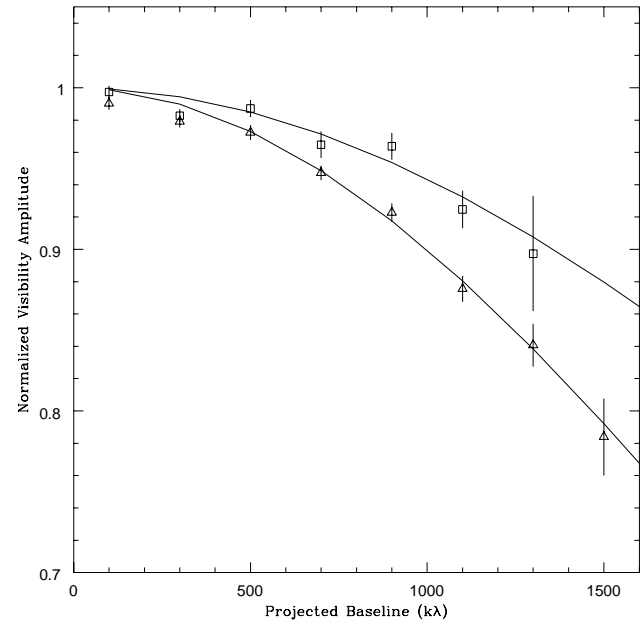
FIG. 7.—Bin-averaged VLA U-band visibility amplitudes vs. baseline length. Triangles represent a 20° wide wedge centered on $\phi = +60°$ (east of north), and squares represent an identical wedge at $\phi = -50°$. (Nonperpendicular wedges were chosen to better sample the $[u, v]$ tracks of this observation.)

TABLE 4
FITTED PARAMETERS TO K-, X-, AND L-BAND OBSERVATIONS[a]

PARAMETERS	VLA K BAND[b]		VLBA X BAND[b]	VLA L BAND
	Amplitude	Closure Amplitude	Amplitude	Image
θ_{maj} (mas)[b].....................	14 ± 2	11 ± 2	110 ± 10	3930 ± 15
θ_{min} (mas).....................	...	...	...	3014 ± 18
ρ	...	...	...	1.30 ± 0.01
ϕ (degrees east of north)......	...	...	...	98 ± 1
S_0 (mJy)	662 ± 3	...	400 ± 60	365 ± 1

[a] α fixed at 1.95 for the K and X bands, 2.0 for L band (Gaussian fit).
[b] K and X bands fitted to circular model.

(length = 3.4 Mλ), which had an rms visibility amplitude of 200 mJy. We use this point to estimate the flux density of NGC 6334B at K band to be approximately 250 mJy in 1993 April, assuming $\theta_s \sim 15$ mas. Alternatively, if we assume a flux density of 400 mJy, which is the value obtained from fits to the VLBA X-band data (§ 4.5), then the east-west angular size of the scattering disk would be about 30 mas. These conclusions are highly uncertain, however, due to the poor sampling of the visibility function. We note that the K-band scattering disk may be quite elongated, since it samples a smaller and possibly more coherent region of the magnetized plasma screen (see § 6.2).

4.4. P Band

At P band the expected scattering-disk size of NGC 6334B of $\theta_s \sim 1\rlap{.}{''}3$ means that it would be highly resolved on baselines greater than 2.5 km. At this frequency, the region around the source is dominated by free-free emission from the large H II complex NGC 6334. Figure 8 shows our P-band image of the region. This image was created by using the maximum entropy deconvolution method (MEM), as implemented by the AIPS routine VTESS. The bipolar H II region NGC 6334A is indicated, as is the location of NGC 6334B. This image highlights the difficulty in modeling the scattering region precisely in the crowded field. The area responsible for the scattering of NGC 6334B appears to be in an interstitial region of low emissivity, between the northern lobe of NGC 6334A and a ridge of star formation to the northeast (Rodríguez, Cantó, & Moran 1982). The flux density in the P-band image at this point is less than the lowest (3 $\sigma = 150$ mJy beam^{-1}) contour of the image, which corresponds to a brightness temperature of $T_b \lesssim 760$ K. This implies a P-band opacity of $\tau_P \lesssim 0.08$, assuming an electron temperature of 10^4 K, and gives an upper limit on the emission measure of the

scattering region of 22,000 cm^{-6} pc. This limit on the emission measure is less than the value of 60,000 cm^{-6} pc found by Moran et al. (1990a) from their 6 cm VLA image of the region, and much less than the value of 150,000 cm^{-6} pc found by Schraml & Metzger (1969) from single-dish measurements. We believe that our underestimate of the emission measure is due to resolution by the VLA of extended emission in the NGC 6334 region. Uncertainty in the zero-spacing flux density of our P-band measurements prevents accurate determination of the emission measure from the synthesized image. Taking the Schraml & Mezger (1969) value for the emission measure as an upper limit, the free-free opacity along the line of sight to NGC 6334B is less than 0.5, which implies only a modest amount of absorption. On the other hand, assuming the size of NGC 6334B scales as λ^2, we expect $\theta_s \approx 70''$ at P band. The synthesized beam of the P-band experiment is $41'' \times 33''$, so the scattering disk would be resolved with its flux density in a synthesized image diluted by a factor of 3.6. If we assume a flux of 500 mJy for the quasar, this dilution would render the scattering disk undetectable in our image. We believe that resolution by the interferometer, and not free-free opacity, is the reason for the lack of detection of NGC 6334B with the VLA at P band.

4.5. X Band

We have X-band data from the VLBA + VLA phased array only. At this frequency, the expected size of the NGC 6334B scattering disk is approximately 100 mas, and we expected it to be highly resolved on VLBA baselines longer than about 75 km (2 Mλ). The shortest projected baseline in this observation was VLA-PT, which varied from 39 to 52 km. The visibilities on this baseline decreased from ~ 130 to ~ 70 mJy over this range (Fig. 9a). The noise level on this baseline, which was averaged in the correlator to 5 s segments, is $\sigma \approx 8.6$ mJy. Hence, $s \sim 8$ on the longest VLA-PT separation. A fit of a circularly symmetric model to the PT-VLA visibility amplitudes gave an X-band flux density of $S_0 = 400 \pm 60$ mJy, and an FWHM angular size of $\theta_s = 110 \pm 10$ mas, for α fixed at 1.95. These results are summarized in Table 4. The angular size is consistent with the expected λ^2 scaling; given that $\theta_s \sim 300$ mas at 6 cm, we would expect $\theta_s \sim 110$ mas at 3.6 cm.

Even after noise-bias removal, there appears to be a significant residual signal on the longer VLA + VLBA baselines in Figure 9a. To confirm the reality of this signal, we performed the statistical analysis described in the Appendix to calculate S/N on these baselines. The results are plotted in Figure 9b. There appears to be a signal at the $s \sim 2$ ($\mathcal{V} \sim 20$ mJy) level present all the way out to baselines nearly 50 Mλ (1800 km) in length. To ensure that this signal was real, and not an artifact of our statistical routine, we performed an identical analysis on artificial data sets, generated by adding Gaussian random noise of magnitude $\sigma = 8.6$ mJy to a set of points computed by using the model in Table 4 and the (u, v) tracks of the VLBA-VLA baselines in our observation. Figure 9b also shows the computed S/N for each scan of a typical artificial data set. While there are spurious "detections" at the 1 σ level, there is no indication that a steady 2 σ signal can be artificially produced from noise alone. We conclude that the low-level visibility-amplitude excess on long baselines in X band is real. In § 6.1.2 we discuss this result in light of the predictions of Goodman & Narayan (1989).
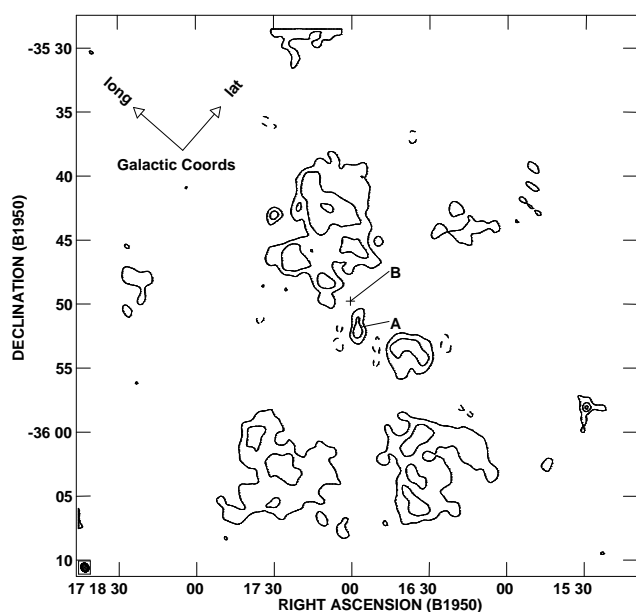

FIG. 8.—VLA maximum entropy P-band (96 cm) map of the NGC 6334 region, from data taken in 1989 March. The contours are at -1, 1, 2, and 3 times the 3 σ noise level of 150 mJy beam^{-1} (beam major axis = 41", minor axis = 33", position angle = 22°). The positions of NGC 6334B and the bipolar H II region NGC 6334A are indicated. The axes in the upper left-hand corner show the orientation of the Galactic plane relative to this region.
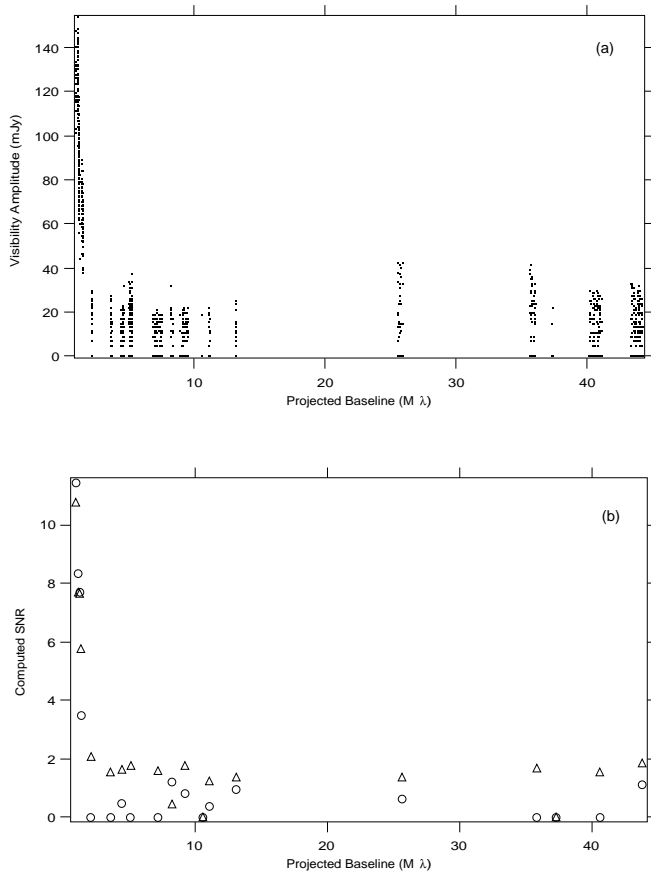
FIG. 9.—(a) VLBA X-band visibility amplitudes measured in 1993 April, averaged to 5 s, on those baselines including the VLA phased array. Bias was corrected for a median noise level of $\sigma = 8.6$ mJy. (b) S/N vs. baseline length, computed by using the technique described in the Appendix, for VLBA X-band data (*triangles*) and simulated data computed using a circular power-law model with $\theta_s = 110$ mas, $S_0 = 400$ mJy (Table 4), and a noise level of 8.6 mJy (*circles*).
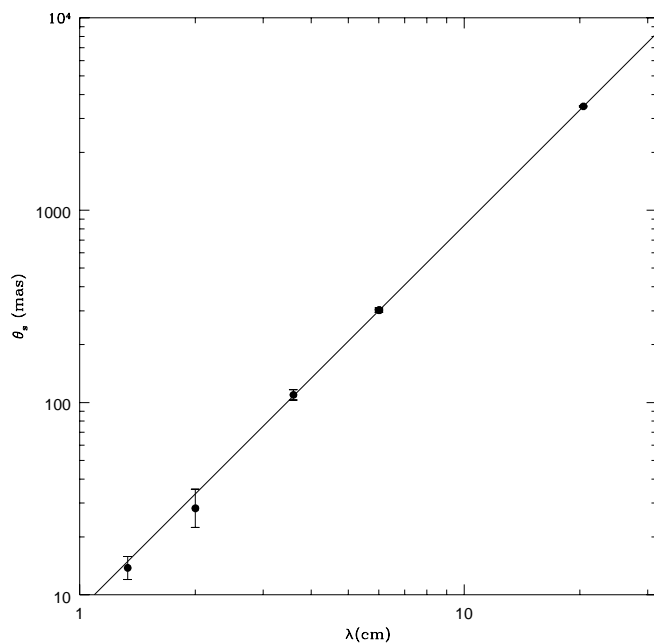

FIG. 11.—Plot of scattering-disk axial ratio ρ vs. wavelength

4.6. L Band

At L band the area around NGC 6334B is filled with free-free emission from the extensive H II clouds in the region. This confusing emission makes it difficult to fit a simple model to the visibility data directly. We chose to restrict the L-band analysis to an elliptical Gaussian brightness profile fitted to a synthesized image (the image is essentially identical to that presented in Rodríguez et al. 1982, and is not reproduced here). The results of our fit are summarized in Table 4. We used the AIPS task IMFIT on a MEM deconvolved image to determine that the L-band scattering disk is also anisotropic, with major axis $\theta_{\mathrm{maj}} = 3930 \pm 15$ mas, minor axis $\theta_{\mathrm{min}} = 3014 \pm 18$ mas, position angle $\phi = 98^\circ.4 \pm 1^\circ$, and an integrated flux density of 365

FIG. 10.—Plot of log θ_m vs. log λ, where $\theta_m \equiv (\theta_{\mathrm{maj}}, \theta_{\mathrm{min}})^{1/2}$. The solid line is the best least-squares linear fit to the data; it has a slope of 2.01 ± 0.01.
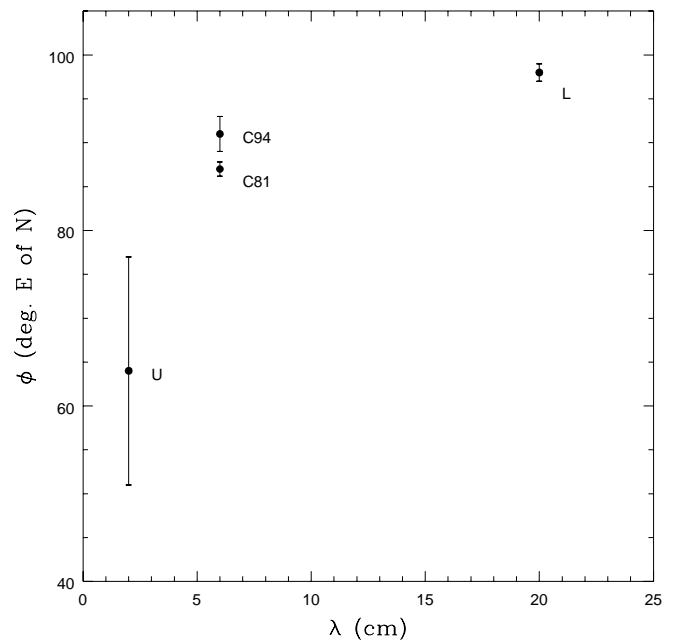
FIG. 12.—Plot of scattering-disk position angle (degrees east of north) vs. wavelength.

mJy. (Because this was a Gaussian fit, the power-law index was fixed at $\alpha = 2$.) This axial ratio ($\rho = 1.3$) and position angle are nearly the same as those in the C band, even though the disk samples an area more than 100 times greater on the scattering screen. The implications of this result are discussed in § 6.2.

4.7. Summary of Wavelength Dependence of Scattering Disk

Figure 10 is a log-log plot of scattering-disk size versus observing wavelength that summarizes our results. For those wavelengths where the scattering disk was found to be elliptical, we plot the geometric mean of the major and minor axes; the error bars take into account the ellipticity as well as errors in the fit. The angular size of the scattering disk is expected to have a power-law dependence on wavelength. The power-law exponent is equal to $1 + 2/\alpha$ for wavelengths at which $r_d \ll r_{in}$, and is equal to 2 for those at which $r_d \gg r_{in}$, where $r_d \approx \lambda/\theta_s$ is the diffractive scale and r_{in} is the inner scale of the turbulence (§ 5.2; WNS). For wavelengths at which $r_d \sim r_{in}$, there should be a smooth transition between these power-law exponents. A least-squares fit to $\log \theta_s$ versus $\log \lambda$ gives a slope of 1.997 ± 0.008, corresponding to a power-law index of $\alpha = 2.01 \pm 0.02$, which is consistent with $\alpha = 2$. This suggests that at least some of the diffractive scales we determined in our range of observing wavelengths satisfy the condition $r_d \gg r_{in}$. The maximum diffractive scale we observed was at K band, where $r_d \approx 5 \times 10^6$ cm. We thus place a conservative lower limit on the inner dissipative scale of turbulence toward NGC 6334B of $r_{in} \gtrsim 5 \times 10^6$ cm.

Figures 11 and 12 show the wavelength dependence of the axial ratio ρ and the position angle ϕ, respectively, for those wavelengths (L, C, and U bands) where ellipticity was confirmed. These plots illustrate the general trends we have found in the wavelength dependence of the shape of the scattering disk: (1) *the axial ratio appears to increase with decreasing wavelength*; and (2) *the position angle appears to rotate with wavelength*. The only other source known to exhibit such wavelength-dependent anisotropic scattering is Cygnus X-3 (WNS).

5. THEORETICAL MATTERS

In this section we review relevant aspects of the physical nature of interstellar turbulence, the theory of radio-wave scattering by a turbulent plasma, and the observable quantities accessible to radio interferometry that give information about the spectrum, scales, and distribution of this turbulence.

5.1. The Nature of ISM Turbulence

The turbulence responsible for radio-wave scattering in the ISM can be described by its three-dimensional density-fluctuation power spectrum, $P_{3N}(k)$, which characterizes the distribution of turbulent cells of size $r = 2\pi/k$, where k is a three-dimensional wavevector. It is usually assumed that the power spectrum takes the form of an unbroken power law between the inner and outer spatial scales of the turbulence, $r_{in} = 2\pi/k_{in}$ and $r_{out} = 2\pi/k_{out}$, with a break at the outer scale and an exponential cutoff at the inner scale (e.g., Narayan 1988). Thus, for isotropic turbulence

$$P_{3N}(k) = C_N^2 (k^2 + k_{out}^2)^{-\beta/2} e^{-k^2/k_{in}^2}, \qquad (6)$$

where C_N^2 is a constant that describes the strength of the fluctuations, and β is a constant. Most observations suggest

a power-law index $11/3 \lesssim \beta \lesssim 4$ (WNS; Armstrong, Rickett, & Spangler 1995; Gwinn et al. 1988). A value of 11/3 corresponds to Kolmogorov turbulence, which describes fluctuations in an incompressible fluid. Theoretical models (e.g., Higdon 1984, 1986; Sridhar & Goldreich 1994) indicate the Kolmogorov model may apply to the ionized ISM as well. Estimates for the inner and outer scales vary. Jokipii (1988) used the measured energy spectrum of Galactic cosmic rays, which he assumed were accelerated by shock fronts in supersonic turbulence, to conclude that in the diffuse component of the ISM the power spectrum of turbulence takes the form of an unbroken power law from scales as small as 10^9 cm to as great as the scale height of the gas in the Galactic disk ($\sim 10^{21}$ cm). WNS used measurements of the scattering disk of Cygnus X-3 to determine a range of $10^7 < r_{in} < 10^{10.5}$ cm, which is in agreement with Jokipii's results; however, their estimate of $r_{out} \sim 0.01$ pc indicates that regions of enhanced turbulence, like those toward Cygnus X-3 and NGC 6334B, may not have the same outer scale as the diffuse component of the ISM.

Recently, evidence has been found that indicates that the turbulent–density-fluctuation spectrum may be anisotropic in some scattering regions (Sgr A*: Backer et al. 1993, Yusef-Zadeh et al. 1994; Cyg X-3: WNS, Molnar et al. 1995; W49: Desai, Gwinn, & Diamond 1994). While it is generally assumed that magnetic fields are responsible for this effect, it is not understood how the field actually induces the anisotropy. If structures in the scattering region are elongated in a particular direction, then the scattering disk of a background source will be oriented perpendicularly to that direction (in analogy to the way a diffraction grating scatters light preferentially in directions perpendicular to its etching). A magnetic origin for anisotropic scattering is supported by observations of the scattering disk of the radio source 3C 279 in the solar corona, which was highly elliptical and oriented perpendicularly to the radial solar magnetic field lines (Narayan & Goodman 1989; Armstrong et al. 1990). Sridhar & Goldreich (1994) and Goldreich & Sridhar (1995) have developed a description of compressible plasma turbulence in the presence of a magnetic field that attributes the distribution of density fluctuations to four-component interactions of shear Alfvén waves. Their model supports a "critically balanced cascade," or equilibrium between wave periods and four-component interaction timescales, that resembles Kolmogorov turbulence in incompressible fluids. They predict that passive density structures (Higdon 1986) will be stretched by this turbulence along the magnetic field lines; an entropy cell with a wavevector component $k_\perp$ perpendicular to the magnetic field in a turbulent region with an outer scale r_{out} will have an axial ratio $\rho \sim (k_\perp r_{out})^{1/3}$. This ratio can approach 10^3 in the ionized ISM, which suggests the density fluctuations in the magnetized plasma are distributed in filamentary structures.

5.2. Radio Scattering in Turbulent Plasma

When a plane wave front from a background source traverses a region of turbulent plasma, it is crinkled by phase distortions. These phase perturbations can be measured by a radio interferometer and, if the intrinsic structure of the source is known, inverted to describe the density structure of the intervening medium.

We discuss the scattering in terms of the geometry of Figure 1. We use the thin-screen approximation, which is

equivalent to the assumption that the thickness of the scattering region is much less than the distance from it to the background source ($L \ll D_{SB}$). In the case of NGC 6334B, D_{SB} is probably greater than several megaparsecs, while $L \sim 1$ pc, corresponding to the path length through the Galactic H II region NGC 6334A. The two-dimensional phase structure function,

$$D_{2\phi}(r) = \langle [\phi(r_0) - \phi(r_0 + r)]^2 \rangle , \qquad (7)$$

describes the phase difference between two points, on the scattering screen or in the observing plane, separated by r. The *diffractive scale* r_d is defined as the magnitude of the vector for which the phase structure function is equal to 1 radian, $D_{2\phi}(r_d) = 1$. The ensemble average complex visibility is related to the two-dimensional phase structure function by the relation

$$\langle V(r) \rangle = S_0 e^{-(1/2)D_{2\phi}(r)} \qquad (8)$$

(Tatarskii & Zavorotnyi 1980), where S_0 is the total flux density of the source. Thus, a point source appears smeared out into a scattering disk of angular size $\theta_s \propto \lambda/r_d$. The diffractive scale can be expressed as

$$r_d \approx \lambda \left(\frac{\theta_s}{7\overset{''}{.}73 \times 10^4} \right)^{-1} , \qquad (9)$$

for $\beta = 4$ ($\alpha = 2$). The exact wavelength dependence of the diffractive scale, and hence the observed size of the scattering disk, depends on the functional form and scales of the turbulent electron density power spectrum. The *refractive scale* r_r is defined in terms of r_d and the Fresnel scale $r_F \equiv (\lambda D_{OS}/2\pi)^{1/2}$ by

$$r_r \equiv r_F^2/r_d , \qquad (10)$$

where D_{OS} is the distance from the observer to the scattering screen. The refractive scale is thus approximately the physical size of the scattering disk on the scattering screen. Assuming that the source is intrinsically unresolved (which is almost certainly the case for NGC 6334B in the VLA observations), density fluctuations on the scale of r_r will focus and defocus the wave front, resulting in brightness variability on timescales of r_r/v_t, where v_t is the tangential relative velocity between screen and observer (Rickett 1986). This effect may be partly responsible for the $\sim 40\%$ decrease of the flux density of NGC 6334B observed at C band (§ 4.1). In this case, the approximate timescale for refractive scintillation $\approx D_{OS} \theta_s/v_t \sim 50$ yr, assuming $v_t \sim 50$ km s^{-1}. Thus, it is conceivable that refractive scintillation is at least partly responsible for the observed flux density variation.

The scales defined above are correct in the limit that the screen–background-source distance is much greater than the observer-screen distance, $D_{SB} \gg D_{OS}$. If the source is positioned closer behind the screen, then we must rescale according to

$$D_{OS} \to \left(\frac{D_{SB}}{D_{OS} + D_{SB}} \right) D_{OS} ,$$

and any vector r in the (x, y)-plane according to

$$r \to \left(\frac{D_{SB}}{D_{OS} + D_{SB}} \right) r .$$

A background source C very close to the scattering screen will have a scattering disk of angular size smaller than that of a very distant background source B

$$\theta_{s, C} = \left(\frac{D_{SC}}{D_{OS} + D_{SC}} \right) \theta_{s, B} . \qquad (11)$$

This screen-source distance "lever arm" effect is used in § 6.4 to constrain the location of a cluster of water masers that lie along the same line of sight as NGC 6334B.

5.3. The Phase Structure Function

The two-dimensional phase structure function $D_{2\phi}(r)$ can be related to the power spectrum of turbulent density fluctuations in the scattering screen (e.g., Rickett 1990). For a scale-free isotropic power-law form of the density-fluctuation power spectrum (eq. [6], with $k_{out} \to 0$, $k_{in} \to \infty$) in a thin screen of thickness L, the two-dimensional phase structure function is given by

$$D_{2\phi}(r) = 8\pi r_e^2 \lambda^2 C_N^2 L f(\alpha) r^\alpha , \qquad (12)$$

where $\alpha \equiv \beta - 2$, and $f(\alpha)$ is a constant of order unity, equal to 0.42 for Kolmogorov turbulence. The phase structure function is proportional to r^α, so by measuring $D_{2\phi}(r)$ over a suitable range of baselines the power-law index of turbulent density fluctuations can be estimated. With a phase structure function of the form of equation (12), the diffractive scale depends on wavelength as $r_d \propto \lambda^{2/\alpha}$. Thus, the angular size of the diffractive scattering disk scales as $\theta_s \propto \lambda^{1+2/\alpha}$. Note that these scaling relations are only strictly valid for a scale-free phase structure function. Narayan & Hubbard (1988) generalized the phase structure function analysis outlined above to allow for anisotropic scattering.

For isotropic density fluctuations with an inner cutoff r_{in} and an outer cutoff r_{out} as given in equation (6), the corresponding phase structure function is

$$D_\phi(r) \propto \begin{cases} r_{in}^{\alpha-2} r^2 , & r < r_{in} , \\ r^\alpha , & r_{in} < r < r_{out} , \\ r_{out}^\alpha , & r > r_{out} . \end{cases} \qquad (13)$$

Hence, on baselines shorter than r_{in} the visibility profile of the scattering disk will be Gaussian ($\alpha = 2$). It is not feasible to probe the outer scale directly with an interferometer, although it is possible to place some constraints on r_{out} by using multifrequency observations of an elliptical scattering disk. WNS use the difference in ellipticity and orientation of Cygnus X-3 between 408 and 1692 MHz to estimate $r_{out} \sim 0.003$ pc, assuming that the changes in the disk with frequency were due to the resolution of the correlation scale of the magnetic field in the scattering screen. In § 6.2 we use our measurements at U, C, and L bands to make a similar estimate of r_{out} toward NGC 6334B.

5.4. Interferometric Visibilities

If the conditions for the ensemble average are not met, then the visibility will not have the simple form of equation (8). Narayan & Goodman (1989) identify three regimes of time averaging for visibilities measured on a baseline of length r, assuming infinitesimal receiver bandwidth and background-source size: snapshot, $t_{int} < r_d/v_t$; average, $r_d/v_t \ll t_{int} \ll \lambda D_{OS}/rv_t$; and ensemble average, $t_{int} \gg \lambda D_{OS}/rv_t$. For example, with $\lambda = 1$ cm, $r \sim 10^8$ cm, $D_{OS} = 1.7$ kpc, and $v_t \sim 30$ km s^{-1}, t_{int} would have to be longer than a year to achieve a true ensemble average and shorter than a few seconds to qualify as a snapshot.

Narayan & Goodman (1989) investigated the properties of the average complex visibility through numerical simulations of observations and by analytical calculation of the rms visibility amplitude $\mathscr{V}_{\mathrm{rms}}$ and its higher moments. They find that in this time-averaging regime $\mathscr{V}_{\mathrm{rms}}$ does not fall off exponentially with increasing baseline as the ensemble average visibility amplitude does. On baselines greater than the diffractive scale r_d, they predict a "fractal tail" in $\mathscr{V}_{\mathrm{rms}}$ that is due to unresolved substructure in the scattering-disk intensity profile that would be smoothed out in a true ensemble average. The precise strength and baseline dependence of this excess visibility tail depends on details of the power spectrum of the turbulence: the presence of inner and outer scales, the value of the power-law index in the inertial cascade, and the diffractive and refractive scales of the scattering screen. For example, the excess long-baseline rms visibility will be relatively high for scattering by a plasma with a steep spectrum of turbulence ($\beta > 4$), and it increases monotonically with increasing r_{in}. In § 6.1.2 we examine the visibility function of NGC 6334B on very long baselines in light of the predictions of Narayan & Goodman (1989).

6. DISCUSSION

6.1. The Inner Scale of Turbulence

6.1.1. The Power-Law Index of Turbulence

Fits to the C-band VLA data (which were of the best quality of all of our sets) imply a power-law index of the phase structure function $\alpha = 1.95 \pm 0.03$. A linear fit to $\log \theta_s$ versus $\log \lambda$ (§ 4.7) implies a power-law index of $\alpha = 1.997 \pm 0.008$. These results are consistent with a phase structure function power-law index of $\alpha = 2$. Moran et al. (1990b) arrived at the same conclusion based on circular model fits to the 1981 C-band data.

A value of $\alpha = 2$ derived from a fit to the visibility as a function of wavelength is expected if the interferometer baselines sample scales less than the inner scale, $r < r_{\mathrm{in}}$ (eq. [13]). This implies that r_{in} is most likely greater than the longest VLA A-array baselines (≈ 35 km). The value of $\alpha = 2$ derived from the fit to scattering-disk size versus wavelength implies that the inner scale is much greater than the diffractive scales sampled in our wavelength range, $r_{\mathrm{in}} \gg r_d$. The largest diffractive scale sampled is at K band, where $r_d \sim 70$ km (eq. [9]). Based on these two estimates, we place a lower limit on the inner scale of $r_{\mathrm{in}} \gtrsim 5 \times 10^6$ cm. This is consistent with limits on r_{in} determined for other lines of sight; for instance, Molnar et al. (1995) estimate the inner scale toward Cygnus X-3 is on the order of 300 km.

6.1.2. The Fractal Tail

We used the technique described in the Appendix to estimate the scan-averaged rms visibility amplitudes for the X-band VLBA observation (§ 4.5). We found that the longer baselines ($r \gg r_d$; $r_d \approx 3 \times 10^6$ cm at X band) seem to show residual visibility amplitudes in excess of those expected for the exponential ensemble average scattering-disk model (eq. [8]). This may be due to the effects of incomplete realization of the ensemble average and/or an inner scale to the turbulence, as discussed by Goodman & Narayan (1989) and Narayan & Goodman (1989). The integration time and bandwidth of these observations correspond to the "average visibility" regime. If the average visibility function varies significantly over the length of a

scan, the technique described in the Appendix could underestimate the rms amplitude, since these variations cannot be distinguished from measurement noise and may result in overcorrection of the amplitude bias. Variations in the average visibility function will be significant if the baseline rotates by more than r_d/b radians over the length of the scan, where b is the baseline length (Narayan & Goodman 1989). Our longest X-band VLBA baselines meet this criterion; however, the magnitude of this effect is probably negligible compared with the inherent errors in the estimates. Given these uncertainties, it is difficult to compare our results quantitatively with the models of Goodman & Narayan. A rough comparison of our results with their theoretical curves, assuming a Kolmogorov spectrum of turbulence (Fig. 7 of WNS), implies that $\log (r_{\mathrm{in}}/r_d) \lesssim 5-6$, or $r_{\mathrm{in}} \lesssim 10^{11-12}$ cm. More sensitive measurements on these scales, especially in the unsampled region from 1.5 to 5 Mλ (50 to 180 km) could allow modeling of the visibility excess as a function of r_{in} and α. Note that our upper limit on r_{in} agrees roughly with the limit $r_{\mathrm{in}} < 10^{10.5}$ cm estimated for Cygnus X-3 (WNS).

6.2. The Outer Scale of Turbulence

Between the C and U bands, the axial ratio of the scattering disk of NGC 6334B appears to increase, and the position angle appears to rotate. A larger axial ratio and position angle shift at high frequencies could be understood if the projected magnetic field direction in the plane of the sky varies on scales comparable to the U-band refractive scale ($\sim 10^{14}$ cm). The scattering disk samples an area of the scattering screen in U band that is 100 times smaller than in C band. Variations in the projected magnetic field direction that are averaged over the C-band scattering disk may be resolved by the smaller U-band disk. This effect is illustrated in Figure 13.

In contrast, the L-band scattering disk has nearly the same position angle and ellipticity as the C-band disk. Since the ellipticity doesn't decrease from C band to L band, while the area sampled on the screen increases by a
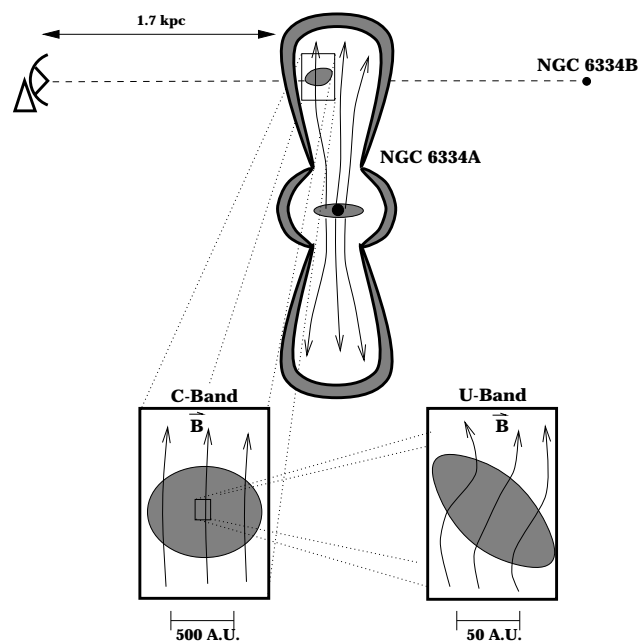

FIG. 13.—Model of the scattering region of NGC 6334B

factor of 100, there appears to be an *outer scale* to the magnetic turbulence, beyond which there are no significant random perturbations on the mean projected field direction. An upper limit for this outer scale is the refractive scale at C band, $r_r \sim 10^{16}$ cm. Theoretical models of magnetohydrodynamic turbulence (Higdon 1984, 1986; Sridhar & Goldreich 1994; Goldreich & Sridhar 1995) indicate that the outer scale of the turbulent density fluctuations r_{out} and the coherence scale of magnetic field fluctuations should be similar. We interpret the frequency dependence of the scattering-disk orientation and shape to indicate that $r_{out} \lesssim 10^{16}$ cm. This value for the outer scale of turbulent density fluctuations toward NGC 6334B is comparable to the value determined by WNS toward Cygnus X-3. An alternative explanation for the change in ellipticity and position angle at higher frequencies may be that we are resolving structure intrinsic to the background quasar. More high-resolution, high-frequency observations of NGC 6334B would help to clarify this issue.

The magnetic coherence scale interpretation would be supported by observations that show a further change in shape and orientation from U band to K band, or that show changes in time as the transverse motion of the screen allows us to sample new regions of the scattering medium. The refractive scale at U band is only about 50 AU. Given an outflow velocity $v \sim 30$ km s^{-1} (De Pree et al. 1995), a new region of the scattering medium will be sampled about every 10 yr. The U-band observations we examined were taken in 1981. Another observation of NGC 6334B at this frequency might serve to further constrain the parameters of the scattering-screen model.

We note that this upper limit on the outer scale disagrees with measurements made of the turbulence in the diffuse Galactic disk component of the interstellar medium. Jokipii (1988) analyzed the energy spectrum of Galactic cosmic rays and concluded that the outer scale for turbulence in the diffuse ISM may be as large as 10^{19} cm. However, regions of enhanced scattering differ markedly from the diffuse ISM in the Galactic disk. In the case of Cygnus X-3, the scattering appears to be due to an H II region that is part of an expanding shell centered on the Cyg OB2 association (Molnar et al. 1995). Similarly, the scattering region of NGC 6334B appears to be associated with the H II region NGC 6334. The outer scale of turbulent density fluctuations is thought to correspond to the scale at which turbulent energy is injected into the medium. It seems reasonable to assume that the physical process powering the turbulent cascade in dense regions of active star formation, and hence the outer scale, differs from that in the diffuse Galactic ISM.

6.3. Modeling the Scattering Screen

NGC 6334 is a giant complex of molecular clouds, H II regions, and sites of active star formation that lies a distance of $D = 1.7$ kpc (Rodríguez et al. 1982). Embedded in this region is the bipolar H II region NGC 6334A, which appears to be associated with outflow from a young star cluster (RCM). VLA observations of radio recombination lines (De Pree et al. 1995) indicate an outflow velocity of $v_{out} \sim 30$ km s^{-1} along the extended lobes, based on an inclination $i = 10°$, and a velocity gradient in the core consistent with Keplerian rotation about a mass of ~ 300 $M_\odot$. The H II lobes extend about 2′ (1 pc) along a north-south axis corresponding to the outflow. Their ionization appears to be due to UV photons escaping from the young star(s) through

"gaps" in the shell-like structure that encloses them (RCM). The bipolar morphology of this H II region is most likely produced by a massive rotating molecular disk that lies in the plane perpendicular to the axis of the lobes (Kraemer et al. 1997). The scattering region of NGC 6334B lies about 2′ (1 pc) from the core of NGC 6334A, at the end of its northern lobe.

If the elongation of the scattering disk is the result of a large-scale magnetic field permeating the medium, then the disk is expected to be oriented perpendicularly to the mean magnetic field direction projected on the plane of the sky (§ 5.1). Given the east-west orientation of the scattering disk of NGC 6334B in the C and L bands, we infer that the mean projected magnetic field in the scattering region, averaged over the C-band refractive scale $r_r = D\theta_s \sim 10^{16}$ cm, is oriented very nearly north-south, along the axis of the bipolar outflow associated with NGC 6334A. Models of magnetically driven outflow from an accreting young stellar object (e.g., Safier 1993; Shu et al. 1988) and observations of magnetic fields in bipolar outflows (Strom et al. 1986) suggest that the magnetic field in the lobes should be generally directed along the axis of the outflow. Our observations support this suggestion.

6.4. High-Velocity H_2O Masers

We looked for evidence of scatter broadening in the H_2O maser features located toward the center of NGC 6334A. Figure 14a shows a map of the angular distribution of these water maser features, and Figure 14b shows the power spectrum. Fits of circular and elliptical Gaussian profiles in the visibility and image planes revealed that none of these features is significantly resolved by the VLBA. Figure 15 shows the cross-power flux density as a function of baseline length for the channel of peak emission. The normalized visibility drops to about 60% on a baseline of 100 Mλ, which implies a source size of $\theta_s \sim 0.5$ mas. Since there appears to be some beating of multiple spectral features in the visibility profile, we set this as an upper limit to the maser feature size. Assuming that the strength of scattering along the line of sight to the maser is comparable to that toward NGC 6334B, we would expect a 1.3 cm scattering-disk size to be about 15 mas for a large source-screen distance ($D_{SB} \rightarrow \infty$). The diffractive scattering angle θ_s decreases with decreasing source-screen distance as $\theta_s \propto D_{SB}/(D_{OS} + D_{SB})$ (eq. [11]). In this case, $D_{OS} \approx 1.7$ kpc. Thus we place an upper limit of a few hundred parsecs on the maser-screen distance D_{SC}. It is plausible that the masers are physically associated with the bipolar H II region NGC 6334A. However, the high line-of-sight velocity of the masers ($v_{LSR} = -80$ km s^{-1}) is somewhat difficult to explain, since the typical outflow velocities in NGC 6334A are on the order of 30 km s^{-1} (De Pree et al. 1995), and the systemic velocity of NGC 6334 is about -10 km s^{-1}. It is very unlikely that the high velocity results from Galactic rotation, since that would require the masers to be at a distance of at least 5 kpc behind the scattering screen, which is incompatible with the upper limit given by the lack of scattering. The features nearly coincide with the western edge of the central shell-like feature observed in maps of NGC 6334A (De Pree et al. 1995; RCM) that has been interpreted as a "bubble" in the surrounding medium inflated by the stellar wind from the young star cluster at the center. If the masers are dynamically associated with the stellar wind, velocities of -80 km s^{-1} are not unreasonable. Stone, Xu, & Mundy (1995) propose a model in which frag-
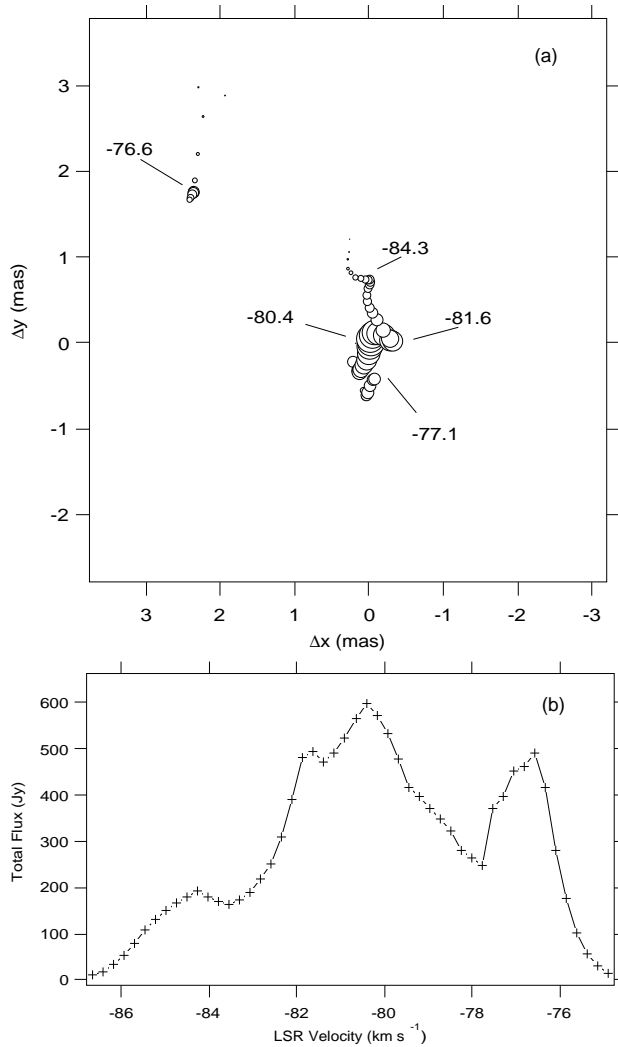
Fig. 14.—(a) Distribution of H_2O maser features near NGC 6334A, observed with the VLBA in 1993 April. Circles indicate all features above 5 σ in the channel maps; the size of the circle is proportional to the flux density. Selected peaks are labeled with their velocities in km s^{-1}. (b) Spectrum created by summing the observed flux densities of features in each spectral channel.

Fig. 15.—Visibility amplitude as a function of baseline length for the H_2O maser peak ($v_{LSR} = -80.4$ km s^{-1}).

ments of a shell surrounding a newly formed star can be ejected at very high velocities by the stellar wind, resulting in supersonic "bullets," or knots of high-density gas that can have speeds of several hundred kilometers per second. The H_2O masers in NGC 6334A may be associated with such a bullet, ejected directly from the shell by the high-speed wind from the young star(s) inside. Given that the emission is blueshifted relative to the ionized gas in NGC 6334A (De Pree et al. 1995), this maser feature probably lies in the foreground of the nebula, which would also help to explain the observed lack of scatter broadening of the features.
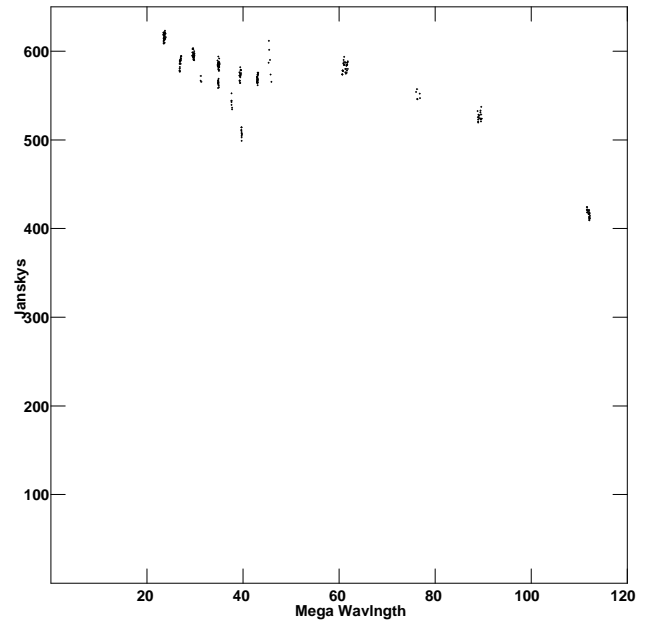
7. CONCLUSION

The scattering disk of NGC 6334B is found to be anisotropic at C and L bands, with a long-to-short axial ratio $\rho \sim 1.2$ and an east-west orientation. This anisotropy implies that the magnetic field in the scattering screen is oriented north-south, along the outflow axis of the bipolar H II region NGC 6334A, located 2' to the south. U-band observations hinted at even larger anisotropy, and showed a shift in position angle of 30°. Such trends in the scattering-disk shape and orientation with frequency are consistent with an outer scale to the turbulent density fluctuations of $r_{out} \lesssim 10^{16}$ cm (0.003 pc). Statistical analysis of X-band visibility amplitudes on long VLBA baselines indicate the presence of excess signal, as predicted by Goodman & Narayan (1989). Based on the magnitude of the visibility excess, we place a tentative upper limit on the inner scale of turbulence of $r_{in} \lesssim 10^{11-12}$ cm. The derived values for the power-law index of the phase structure function are consistent with $\alpha = 2$ for all of our observations, and we place a lower limit on the inner scale of $r_{in} \gtrsim 5 \times 10^6$ cm. High-velocity H_2O maser features along the same general line of sight show no evidence of scatter broadening, suggesting that they are physically associated with the scattering region—perhaps bullets of molecular material ejected from NGC 6334A.

APPENDIX

THE VISIBILITY-AMPLITUDE BIAS AND ERRORS

It can be shown (TMS) that the measured visibility amplitude Z will have a positive bias with respect to the true amplitude

$\mathscr{V}$ given by

$$Z^2 \approx \mathscr{V}^2 + 2\sigma^2 \, , \qquad (14)$$

where σ is the rms deviation of one component of the complex noise vector. Since this bias can be significant in cases of low S/N, we spent considerable effort in exploring ways to accurately account for it, especially in the analysis of the long-baseline visibilities from the VLBA.

We estimated σ directly from the observed distribution of visibility amplitudes. We first distributed the measured visibility amplitudes Z_i into bins. Depending on the instrument and the volume of data, the bins could be rectangular boxes or segmented wedges in the (u, v)-plane (typical procedure with VLA data), or all the data from a particular scan on a particular baseline (more suited to the VLBA, which had baselines of varying sensitivity owing to the inclusion of the phased-array VLA). For each bin we computed the second and fourth moments of the amplitude,

$$\langle Z^2 \rangle \approx \frac{1}{N} \sum_{i=1}^{N} Z_i^2$$

and

$$\langle Z^4 \rangle \approx \frac{1}{N} \sum_{i=1}^{N} Z_i^4 \, , \qquad (15)$$

where N is the number of data points in the bin, and we have approximated the ensemble average by the arithmetic mean over the data bin. $\langle Z^2 \rangle$ and $\langle Z^4 \rangle$ have simple functional dependencies on σ and $\mathscr{V}$. If we define S/N, $s \equiv \mathscr{V}/\sigma$, then

$$\langle Z^2 \rangle / \sigma^2 = s^2 + 2$$

and

$$\langle Z^4 \rangle / \sigma^4 = s^4 + 8s^2 + 8 \qquad (16)$$

(TMS; Rogers, Doeleman, & Moran 1995). With the data and these two equations we can solve for σ^2 and $\mathscr{V}^2$. We performed this solution by taking the ratio $\zeta(s) = \langle Z^4 \rangle / \langle Z^2 \rangle^2$, which is a function of s only. We then used equation (16) to split s into an estimate of $\mathscr{V}^2$ and σ^2. This method becomes inaccurate for very low S/N data. The range of the ratio is $2 > \zeta > 1$ for $0 < s < \infty$. The values of $\langle Z^2 \rangle$ and $\langle Z^4 \rangle$ given by equation (15) will have some distribution about the true ensemble average values, with a width proportional to $N^{-1/2}$. It is possible that for very high or very low S/N we may not be able to use the moment ratio to estimate σ for a given bin, especially if the number of points in that bin is small.

To examine the limits of this technique, we performed Monte Carlo tests on simulated data sets. Using a model such as equation (1) for the source structure and a fixed value or set of values for σ, we generated sets of Z_i with the (u, v) coverage of a typical observation. We found that for $s \gtrsim 3$, this technique is quite accurate, provided that the number of points in a typical data bin $N \gtrsim 50$. For $N < 50$, there is a significant probability that this routine will indicate a low-S/N detection (at the $s \sim 1$ level) in a bin where there is in fact no signal, and the estimates of true low-level signals appear biased to higher values. For $N \sim 50$, this technique will reliably indicate the *presence* of a signal at the 2 σ level or greater, although the computed value of S/N is rather uncertain for $s < 3$.

REFERENCES

Armstrong, J. W., Coles, W. A., Rickett, B. J., & Kojima, M. 1990, ApJ, 358, 685
Armstrong, J. W., Rickett, B. J., & Spangler, S. R. 1995, ApJ, 443, 209
Backer, D. C., Zensus, J. A., Kellermann, K. I., Reid, M. J., Moran, J. M., & Lo, K.-Y. 1993, Science, 262, 1414
De Pree, C. G., Rodríguez, L. F., Dickel, H. R., & Goss, W. M. 1995, ApJ, 447, 220
Desai, K. M. 1995, Ph.D. thesis, Univ. California at Santa Barbara
Desai, K. M., Gwinn, C. R., & Diamond, P. J. 1994, Nature, 372, 754
Goldreich, P. M., & Sridhar, S. 1995, ApJ, 438, 763
Goodman, J., & Narayan, R. 1989, MNRAS, 238, 995
Gwinn, C. R., Moran, J. M., Reid, M. J., & Schneps, M. H. 1988, ApJ, 300, 817
Higdon, J. C. 1984, ApJ, 285, 109
———. 1986, ApJ, 309, 342
Jokipii, J. R. 1988, in AIP Conf. Proc. 174, Radio Wave Scattering in the Interstellar Medium, ed. J. Cordes, B. Rickett, & D. Backer (New York: AIP), 48
Kraemer, K. E., Jackson, J. M., Paglione, T. A. D., & Bolatto, A. D. 1997, ApJ, 478, 614
Molnar, L. A., Mutel, R. L., Reid, M. J., & Johnston, K. J. 1995, ApJ, 438, 708
Moran, J. M., & Rodríguez, L. F. 1980, ApJ, 236, L159
Moran, J. M., Rodríguez, L. F., Greene, B., & Backer, D. C. 1990a, ApJ, 348, 147
———. 1990b, in IAU Symp. Radio Astronomical Seeing, ed. J. Baldwin & W. Shouguan (Beijing: International Academic Publishers), 255

Narayan, R. 1988, in AIP Conf. Proc. 174, Radio Wave Scattering in the Interstellar Medium, ed. J. Cordes, B. Rickett, & D. Backer (New York: AIP), 17
Narayan, R., & Goodman, J. 1989, ApJ, 238, 963
Narayan, R., & Hubbard, W. B. 1988, ApJ, 325, 503
Press, W. H., Teukolsky, S. A., Vetterling, W. T., & Flannery, B. P. 1992, Numerical Recipes in FORTRAN (2d ed.; Cambridge: Cambridge Univ. Press)
Rickett, B. J. 1986, ApJ, 307, 564
———. 1990, ARA&A, 28, 561
Rodríguez, L. F., Cantó, J., & Moran, J. M. 1982, ApJ, 255, 103
———. 1988, ApJ, 333, 801 (RCM)
Rogers, A. E. E., Doeleman, S. S., & Moran, J. M. 1995, AJ, 109, 1391
Safier, P. N. 1993, ApJ, 408, 115
Schraml, J., & Metzger, P. G. 1969, ApJ, 156, 269
Shu, F. H., Lizano, S., Ruden, S. P., & Najita, J. R. 1988, ApJ, 328, L19
Sridhar, S., & Goldreich, P. M. 1994, ApJ, 432, 612
Stone, J. M., Xu, J., & Mundy, L. G. 1995, Nature, 377, 315
Strom, K. M., Strom, S. E., Wenz, M., Wolff, S. C., & Morgan, J. 1986, ApJS, 62, 39
Tatarskii, V. I., & Zavorotnyi, V. U. 1980, Prog. Opt., 18, 204
Thompson, A. R., Moran, J. M., & Swenson, G. W. 1986, Interferometry and Synthesis in Radio Astronomy (Malabar: Krieger) (TMS)
Wilkinson, P. N., Narayan, R. E., & Spencer, R. 1994, MNRAS, 269, 67 (WNS)
Yusef-Zadeh, F., Cotton, W. D., Wardle, M. J., Melia, F., & Roberts, D. A. 1994, ApJ, 434, L63